International Journal of
Turbomachinery
Propulsion and Power

MDPI

Article

Experimental Investigation of an Efficient and Lightweight Designed Counter-Rotating Shrouded Fan Stage

Timea Lengyel-Kampmann [1,*], Jirair Karboujian [1,*], Guillaume Charroin [1,*] and Peter Winkelmann [2,*]

[1] German Aerospace Center, Institute of Propulsion Technology, 51147 Cologne, Germany
[2] German Aerospace Center, Institute of Structures and Design, 70569 Stuttgart, Germany
* Correspondence: timea.lengyel@dlr.de (T.L.-K.); jirair.karboujian@dlr.de (J.K.); guillaume.charroin@uphf.fr (G.C.); peter.winkelmann@dlr.de (P.W.)

Abstract: The German Aerospace Center designed, aero-mechanically optimized and experimentally investigated its own counter-rotating shrouded fan stage in the frame of the project CRISPmulti. Their target and the motivation of this work was, on the one hand, the generation of a highly accurate experimental database for the validation of the modern numerical design and optimization processes, and on the other hand, the development of a new innovative technology for the manufacturing of 3D fan blades made of a lightweight CFRP material. The original CRISP-1m test rig designed by the MTU Aero Engines in the 1980s was reused with the new blading for experimental investigation in the Multistage Two-Shaft Compressor Test Facility (M2VP) of the DLR in Cologne. The evaluation of the steady measurement results and the validation of the numerical simulation based on the pressure and temperature measurement are presented in this paper.

Keywords: counter-rotating fan; experiment; design; validation; CFD

Citation: Lengyel-Kampmann, T.; Karboujian, J.; Charroin, G.; Winkelmann, P. Experimental Investigation of an Efficient and Lightweight Designed Counter-Rotating Shrouded Fan Stage. *Int. J. Turbomach. Propuls. Power* **2024**, *9*, 26. https://doi.org/10.3390/ijtpp9030026

Academic Editor: Antoine Dazin

Received: 12 December 2023
Revised: 15 February 2024
Accepted: 27 February 2024
Published: 3 July 2024

1. Introduction

One of the main targets of engine research is a reduction in fuel consumption to make air traffic more environmentally friendly. Therefore, the counter-rotating fan and propeller concepts awakened the interest of the aircraft engine industry due to the opportunity to achieve higher efficiency. The DLR participated in several international projects dealing with these concepts. Based on this knowledge, the German Aerospace Center has decided to design its own counter-rotating shrouded fan stage and to test it on the CRISP-1m rig [1,2]. The blade geometry was redesigned, the material and the manufacturing technology was improved. Multidisciplinary project targets were striven for:

- The main design goal was to maximize the aerodynamic efficiency under restricted static and dynamic mechanical properties of the blade [3].
- An engine cycle concept should be created and a calculation for an engine with an extremely high bypass ratio should be carried out.
- Weight savings of 30% (structural weight) with modern CFRP blades should be achieved.
- Automatable manufacturing technology for thermoplastic CFRP fan blades should be developed.
- The noise emission of the new fan should not be higher than that of a turbofan for engines of the same thrust class. However, a significant noise reduction is not expected and is not realistic based on past experience. The expected goal here is for the CRISPmulti design to have a 6 dB lower noise emission than the reference CRISP design.
- Experimental investigations should be conducted to validate the optimization results, the FE calculational method and the acoustic properties predicted by the DLR in-house code PropNoise.

During the design phase, an automated multi-objective, multidisciplinary optimization method was applied, which allows the simultaneous use of both a CFD process chain to determine the aerodynamical properties of the fan geometry and also a FE process chain to analyze the structural behavior of the blades and the disc. This FE calculation method of the composite blades is a significant result of the project, which should be validated by the test results.

The instrumentation enables the measurement of the fan aerodynamics by different pressure and temperature rakes and the acoustic measurement by microphones. The unsteady flow field will be characterized by hot wire measurement, optical measurement (PIV) and Kulite measurement.

The experiments on the CRISPmulti rig were extended by inlet distortion measurements in order to investigate the behavior of a Counter-Rotating Turbofan under boundary layer ingestion. The boundary layer of the aircraft fuselage ingested into the engine causes a drop in the total pressure in front of the fan. This is generated on the test rig by a distortion grid combined with a honeycomb downstream of the grid to avoid the generation of tangential flow velocity components. The design of the distortion grid was carried out as part of the project AGATA and is described in detail in another paper [4]. In order to be able to measure the different circumferential positions in the case of the distorted inlet conditions with all the planned measuring techniques, the inlet distortion itself is rotatable in the circumferential direction. A radial traversing device mounted on the rotatable pipe of the inlet channel enables the continuous and slow introduction of the distortion grid into the inflow channel during operation, controlled from the control room.

The measurement campaign was completed in June 2022. In this paper, the experimental setup and the results of the stationary measurement will be described in detail. The target of this paper is to present the validation of the numerical performance map of the CRISPmulti rig based on the measured data. The evaluation of the unsteady measurement with inlet distortion will be presented in further publications.

2. Blade Design and Optimization

Since the design process of the blades is not the main focus of this paper, only the result of the optimization is presented below. A detailed description of the design process was published in [3]. The final blade geometry of the CRISPmulti fan is shown in Figure 1. Since the blades were designed for an existing test rig, some constraints were defined for the design. The exit swirl should be kept close to 0° and the axial Mach number should remain above 0.69, similar to modern aero engines. These constraints and goals are summarized in Table 1.

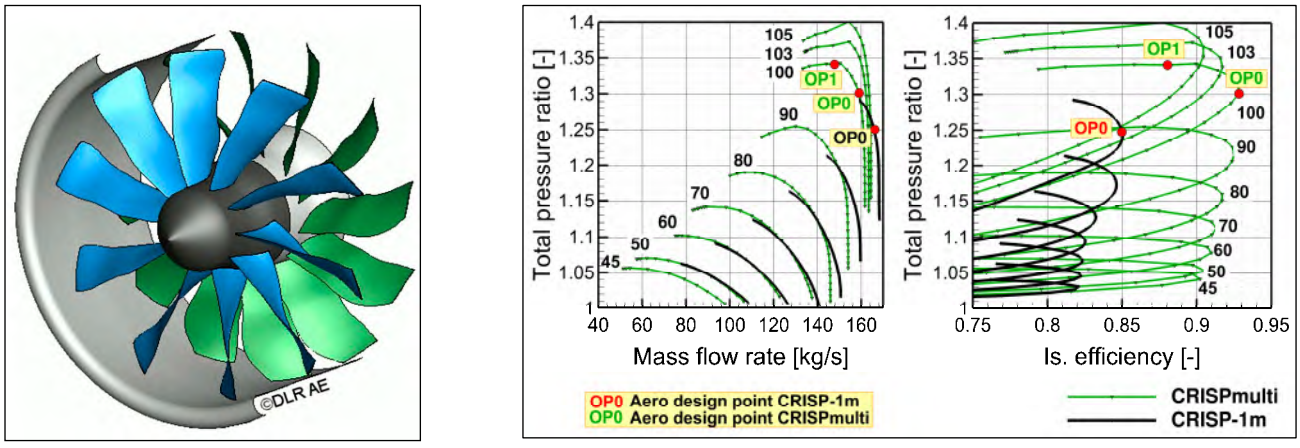

(**a**) (**b**)

Figure 1. The optimized geometry of the fan stage (**a**) and the performance map of the optimized geometry compared with the initial design (**b**) [3].

Table 1. Design constraints, targets and the resulting fan parameter [3].

Design constraints			
Rig constraints	Blade Nr. of Rotor1	10	
	Blade Nr. of Rotor2	12	
	Hub-to-tip ratio	0.27	
	Outer diameter	1 m	
Design goal	Tip clearance at Rotor1 @ADP	0.65 mm	
	Tip clearance at Rotor2 @ADP	0.5 mm	
	Exit swirl @ADP	<3°	
	Axial Mach number	0.69	
Design targets			
		CRISP-1m	CRISPmulti
	Maximize the isentropic efficiency	87%	93%
	Maximize the stall margin	10%	>10%
Optimization results			
		CRISP-1m	CRISPmulti
	Speed ratio (R2 to R1)	0.86	0.79
	100% speed of Rotor1	4980 rpm	5044 rpm
	Fan pressure ratio @ADP	1.25	1.30
	Mass flow @ADP	166	159

The optimization objective is defined as maximizing the efficiency and maximizing the stall margin. The rotational speeds and the fan pressure ratio are considered to be free parameters in the optimization, so the optimum values are set by the optimization. The resulting values are compared in Table 1 with the initial values from the CRISP-1m fan. It is worth noting that the fan pressure ratio was increased to achieve higher efficiencies. The optimum fan pressure ratio for the counter-rotating fan is about 1.3. Figure 1b shows the calculated fan map of the optimized CRISPmulti geometry compared with the map of the initial geometry [2,3].

The final geometry was analyzed by static and dynamic FE simulations in detail.

3. Manufacturing and Experimental Validation of the Blades

The designed blade geometry is provided as a demonstrator for a novel, automatable manufacturing technology for thermoplastic CFRP fan blades, which was developed as part of the Organoblech-CRISP project at DLR. In contrast to the conventional "onion-skin" construction method with individual blanks, the possibility of a thermoplastic base material is used here to produce the aerodynamic blade geometry by forming a so-called "organosheet" onto the skeletal surface of the blades and subsequently by milling (see Figure 2). The design and the manufacturing process are described in detail in the publications [3,5].

(**a**) (**b**)

Figure 2. Manufacturing process of the CFRP blades (**a**) and the shaker test (**b**) [5].

To validate the calculation results, centrifugal tests were carried out on blades for rotors 1 and 2 to determine the static strength. Two rotor 1 blades were centrifuged in the original installation position, with radial alignment of the blade axis of rotation. Since

the test was carried out under a vacuum, the bending moments from the pressure load, which compensate for the bending moments from the centrifugal load at the blade root, were missing here. The test was limited to 100% speed (5045 rpm), but due to the missing compensation, the load in the critical root area was 130% of the calculated load. The blades survived the test without damage. One rotor 2 blade was tested to bursting. The blade reached a speed of 6027 rpm (150%) until failure.

The dynamic strength was verified by shaker tests. For this purpose, 5 blades of rotor 1 and 1 blade of rotor 2 were tested on the institute's own shaker (see Figure 2). The tip amplitude, as the controlled variable of the test, was determined for the first test series in such a way that the acceptable dynamic strain amplitude at the CFRP blade/titanium root transition was found by calculation.

4. Instrumentation

4.1. Target of the Experimental Investigation

The aim of this experiment is firstly to verify the optimization result experimentally and secondly to investigate the effects caused at the fan due to boundary layer ingestion. For this purpose, a high-quality experimental database is to be generated, which will be applied to validate the numerical methods. The experimental investigations are carried out in the M2VP test facility in Cologne, at the DLR Institute of Propulsion Technology. Extensive instrumentation is required to fulfill all measurement tasks. Figure 3 shows a schematic overview of all measurement planes.

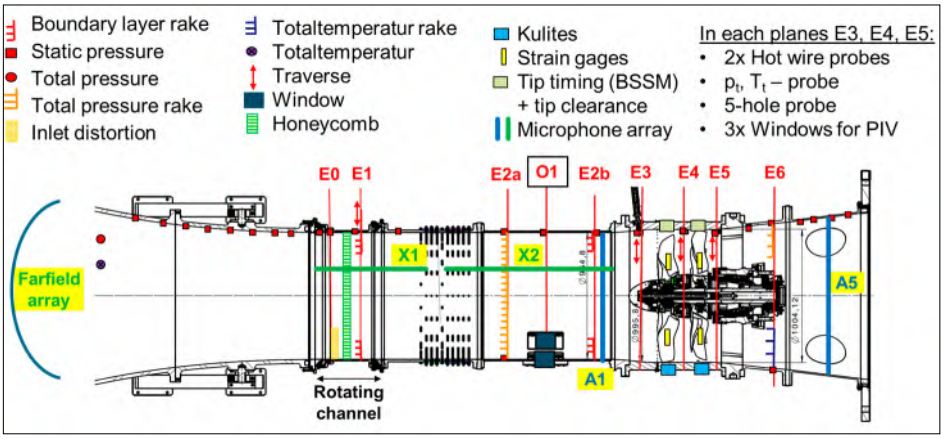

Figure 3. Instrumentation overview.

4.2. Standard Steady Pressure and Temperature Measurement

In the case of the clean inflow, four boundary layer rakes were mounted into the measurement plane E1 to determine the mass flow and the inlet total pressure distribution, applying 41 Pitot tubes in the vicinity of the wall (see Figure 4). The distance between the Pitot tubes was higher with increasing distance from the wall: 1.5 mm, 3 mm, 5 mm and 9 mm. Hot-wire probes could also be inserted between the boundary layer rakes to determine the flow turbulence quantities at the inlet plane. The same boundary layer rakes could also be inserted in the E2b plane in the circumferential positions 45°, 135°, 225° and 315° in order to be able to determine the mass flow when using the honeycomb.

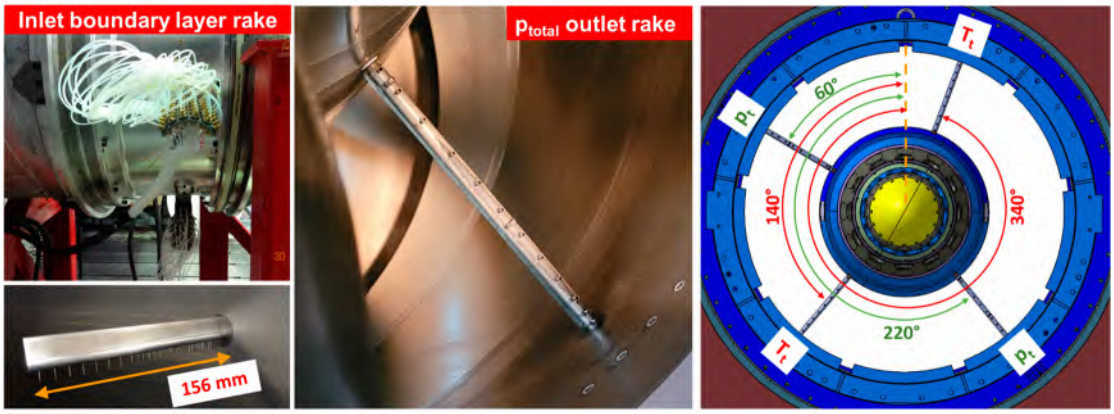

Figure 4. Inlet boundary layer rake (**left**), outlet total pressure rake (**middle**) and the circumferential distribution of the four outlet rakes (**right**).

To determine the total pressure and total temperature distribution downstream of the fan—outlet p_{total} and T_{total}—rakes were used in plane E6 (see Figure 4). Two total temperature rakes with 12 radial measuring points were used in the circumferential positions 140° and 340°. The measuring points were equipped with pt100 resistance temperature sensors. Two total pressure rakes, each with 12 Pitot tubes and 2 three-hole probes, were used in the circumferential positions 60° and 220° in order to determine the total pressure at the outlet and thus the fan pressure ratio. The static pressure was measured at each measurement plane and along the flow channel at several axial positions by 1 mm holes in the casing.

Thus, all in all, over 500 pressure measurement points were recorded in the test rig via a PSI measurement unit. The measured temperatures were recorded by a Delphine data acquisition system. All measured values were displayed and stored with a LabView 2018 program during the measurement.

4.3. Inlet Distortion with the Honeycomb

The pictures in Figure 5 show the honeycomb with the radial traversing device mounted on the rotatable pipe of the inlet channel. A maximum immersion depth of 140 mm is possible. The advantage of this method is that it allows us to apply the distortion only at the stable operating point of the blades. The immersion depth can be controlled and defined afterwards based on the measured effect. In the case of critical blade vibration, the distortion grid can be removed from the channel immediately.

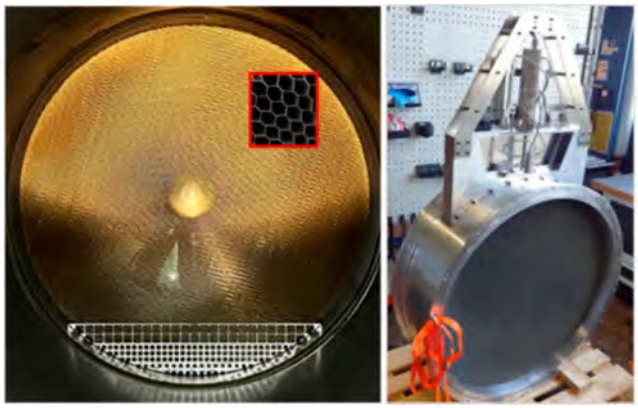

Figure 5. Inlet distortion device.

4.4. Unsteady Measurement Technique for the Online Vibration Monitoring

In addition to the measurement techniques presented before, several sensors were implemented for monitoring the operation of the rig. These all required a high sampling

rate to be able to detect the transient phenomena on the rotating components in time. For this purpose, a high-quality data acquisition system from Dewetron DEWEOrion 1624-200 with 160 channels and a maximum sampling rate of 200 kHz per channel was used. Both rotors were provided with an 8-channel telemetry system for signal transmission from the rotating to the stationary system. On rotor 1, it was possible to transmit the bearing temperatures via 8 additional channels on the telemetry.

To monitor the blade deformation, strain gauges were implemented on the pressure side of the blades. The WK-09-375BG-350 from the manufacturer Vishay from Malvern (Pennsylvania), USA was selected as a suitable strain gauge for application on CFRP blades (see Figure 6). The major challenge in using the strain gauges is the positioning and implementation of the blades. Based on the FEM simulation, 4 positions were determined. One blade was instrumented with 2 strain gauges. Each strain gauge position was used twice, resulting in 8 strain gages per rotor row, distributed over 4 blades.

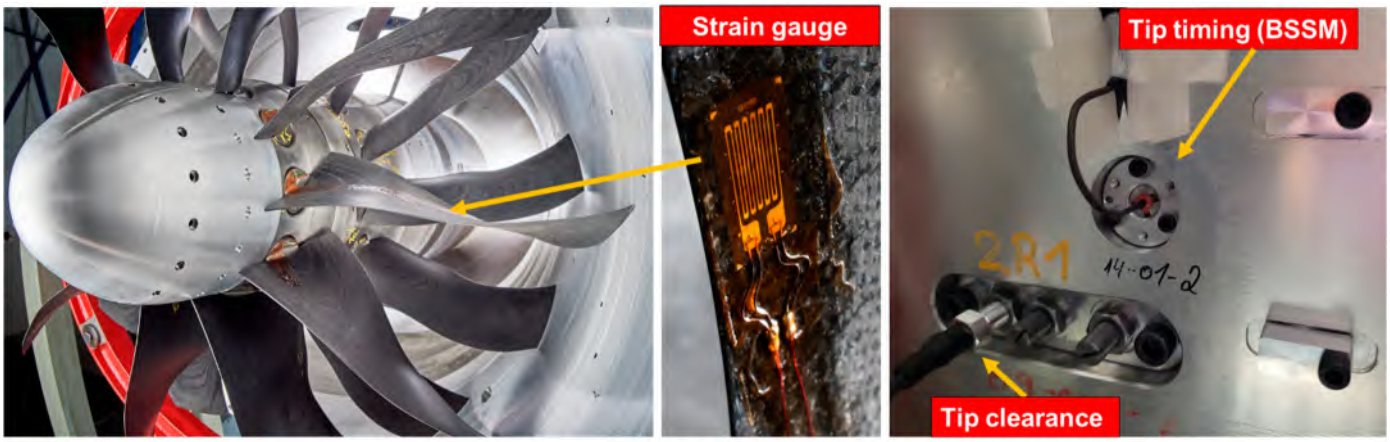

Figure 6. Blade vibration monitoring by strain gauges on the blades (**left** and **middle**) and by capacitive sensors in the casing (**right**).

Further instrumentation for operational monitoring was implemented on the rotor case. DLR's own tip clearance measurement system (Hytron) uses 4 capacitive distance sensors per rotor row (max. 8 channels) to monitor the tip gap during the test. The installation positions in the circumferential direction for both rotors were at 45°, 135°, 225° and 315°. The axial sensor position was determined from the numerical simulations, by finding the position of the minimum tip gap on the fan map. In most cases, these are located at the trailing edge of the blades (see Figure 6).

The entire measurement campaign was supported by the tip timing measurements of the MTU Aero Engines (BSSM—Contactless Blade Vibration Measurement System). This measurement method enables not only the tip clearance but also the blade vibrations to be monitored. A total of 12 capacitive distance sensors were used for this purpose (see Figure 6), which were distributed in the rotor case in two axial positions (2 × 3 pieces) for rotor 1 and in one axial position (6 pieces) for rotor 2.

The monitoring of the rotor dynamic was performed by spectral analysis of the bearing vibration. For this purpose, as many bearing positions as possible in the rig were equipped with accelerometers (type PCB Synotech). The fixed bearings were monitored in all 3 directions (axial, 2× radial) and the floating bearings in 2 radial directions; all in all, 20 sensors were mounted in the test rig.

The rotational speeds (RPM) of both rotors were measured by a so-called trigger sensor from the manufacturer Braun GmbH. The sensor is based on the differential Hall effect. A groove or a hole with a certain width and depth was needed in a steel shaft to obtain a clean square wave signal, from which the rotational frequency could be calculated. A total of 8 sensors were used here for the two shafts: 2 pieces for the 1/rev and 1/blade signals to provide redundancy.

4.5. Special Aero, Structure and Acoustic Measurement Technology

The detailed analysis of the flow field, the blade deformation and the fan acoustics requires the application of special measurement techniques (see Figure 7). IPCT measurements allow the blade deformation to be measured under rotating conditions (see in detail by [6].

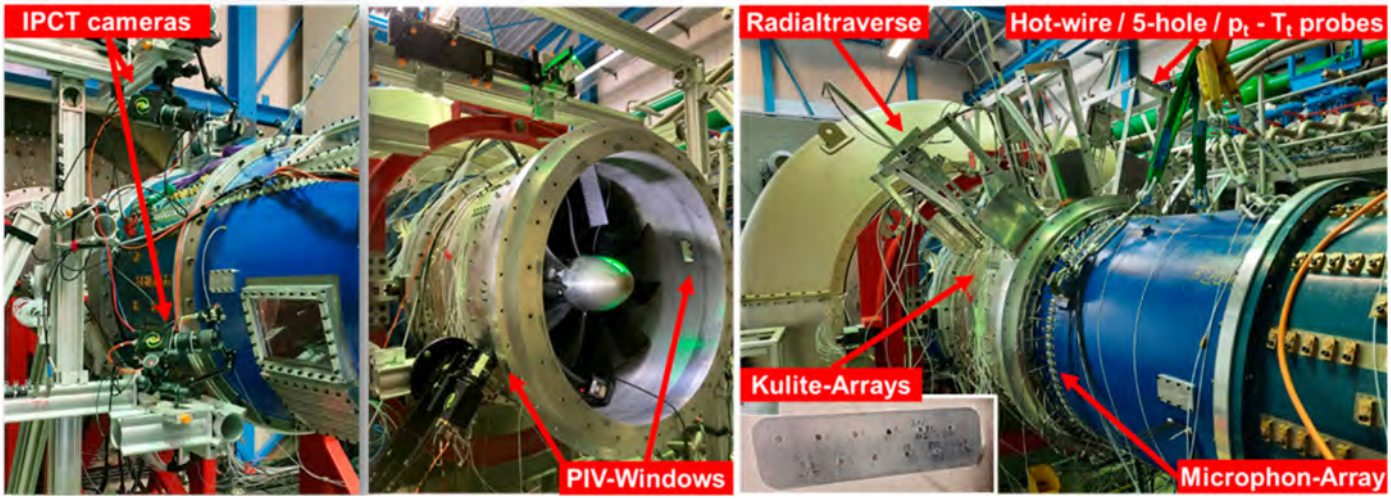

Figure 7. IPCT measurement setup (**left**), PIV measurement setup (**middle**) and the configuration for the combined probe, acoustic and Kulite measurement (**right**).

The measurement techniques to characterize the flow properties were installed in the rotor case, in front of the fan for plane E3, interstage for plane E4 and behind the fan for plane E5. All 3 planes enabled the measurement of the flow velocities by hot-wire anemometry [7] as well as by applying PIV. Flow angles were additionally determined with a 5-hole probe. A Kulite array (12 Kulite sensors in one array) was installed above both rotor rows. Several microphone arrays enabled the measurement of the acoustic behavior of the fan (detailed in [7]).

5. Fan Performance Map Measurement with Clean Inflow

After the commissioning phase, the fan map was measured with the standard instrumentation by installing the BLR in plane E1. Since this plane was located more than 2 m upstream from the fan, the pressure losses of the inlet channel were included in the measured pressure ratios, which led to lower pressure ratios as calculated with the design domain. At the end of the measurement campaign, a more detailed fan map was measured and targeted to achieve the stall margin. In this case, the honeycomb was mounted in plane E1, so the BLRs were installed in plane E2b. The advantages of this configuration are the more homogeneous inflow and lower channel losses.

5.1. Evaluation of the Pressure Measurement

The inlet total pressure was calculated as the area-weighted averaged value of the radial p_t distribution measured by the BLRs. The measured mass flow was determined with the following equation for each ring surface:

$$\dot{m} = \rho \cdot V \cdot A = \frac{p}{R \cdot T} \sqrt{\frac{2}{\kappa - 1} \left(\left(\frac{p_t}{p} \right)^{\frac{\kappa - 1}{\kappa}} - 1 \right)} \cdot \sqrt{\kappa R T} \cdot A \tag{1}$$

where p_t is the total pressure value of the BLRs and p is the static pressure measured at the casing in the same plane. The entire mass flow is calculated as the sum of the individual

mass flows. Basically, the measured performance map (pressure ratio vs. reduced mass flow) is determined only by the pressure measurement with the following equations:

$$\pi = \frac{p_{t,outlet}}{p_{t,inlet}} \tag{2}$$

$$\dot{m}_{red} = \dot{m} \frac{P_{ISA}}{p_{t,inlet}} \sqrt{\frac{T_{t,inlet}}{T_{ISA}}} \tag{3}$$

where T_{ISA} = 288.15 K and p_{ISA} = 101.325 Pa.

5.2. Evaluation of the Temperature Measurement

The temperature measurement was performed by PT100 rakes, which were inserted in the exit flow. Due to the cooling effect of the flow around the Kiel heads, the measured temperature T_{probe} is always lower than the total temperature T_t. Therefore, the application of the recovery factor was necessary to determine the T_t from the following definition:

$$R_k = \frac{T_{probe} - T_s}{T_t - T_s} \tag{4}$$

After the calibration of the recovery factors for all sensor positions at different Mach numbers, the T_s and, with this, the T_t can be calculated. Error sources like heat conduction through the probe and the Kiel head and influences of thermal radiation cannot be determined by the calibration.

The isentropic efficiency is determined based on the total pressure and temperature as follows:

$$\eta_{is} = \frac{\pi^{\frac{\gamma-1}{\gamma}} - 1}{\tau - 1} \tag{5}$$

with $\tau = \frac{T_{t,outlet}}{T_{t,inlet}}$ and γ being the heat capacity ratio for air. Since the uncertainty of the recovery calibration is—depending on the Mach number—relatively high, the error of the efficiency measurement is higher than 1%.

The reduced speed N_{red} is defined by the following equation:

$$N_{red} = \frac{N}{\sqrt{\frac{T^*_{inlet}}{T^*_{ISA}}}} \tag{6}$$

6. Numerical RANS Simulation of the Rig Tests

6.1. Numerical Setup

Using a short calculational domain with a course mesh was recommended for the fan blade optimization to accelerate the CFD calculation in the process chain. This flow path is marked with light blue in Figure 8. On the contrary for the validation, the simulated geometry should be as detailed as possible and meshed with high resolution by applying a low Reynolds grid ($y^+ < 1$). Therefore, the calculational domain was extended to the measurement planes E1 or E2b and E6 where the rakes were positioned, as shown in Figure 8. A commercial mesh generator, AutoGrid5 (developed by NUMECA), was applied to generate the new mesh with hexahedral cells for validation. Adequate mesh quality was achieved with 3.5 million cells in the entire domain.

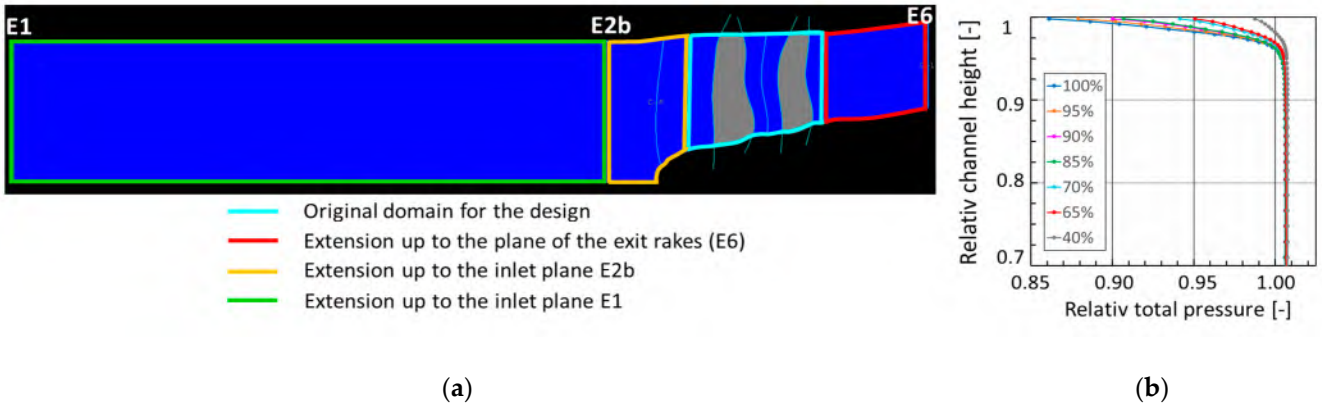

(**a**) (**b**)

Figure 8. Calculational domain for the optimization and for the validation (**a**); Boundary inlet condition based on the measured results (**b**).

6.2. Boundary Conditions

Accurate boundary conditions are very important for the validation of the numerical simulation with the measured data. Accordingly, the measured inlet total pressure with the corresponding boundary layer was applied at the inlet plane for each speed line as a 1D radial distribution (see Figure 8b). The inlet total temperature was measured in the inlet chamber and kept constant for the speed line. Since the boundary layer is calculated as fully turbulent, the turbulent intensity and length scale have no significant effect on the solution. The inlet flow angle was taken as 0°. The outlet boundary condition was defined by the static pressure as radial equilibrium, changing in small steps to calculate the entire speed line. The real measured speeds for both rotors were taken for the simulation.

7. Results and Discussion

The validation results of the CFD calculation based on the fan performance measurement will be presented in this paper. In the first step, a numerical parameter study was carried out to examine the effect of the following parameters on the speed line:

1. Sensitivity of the inflow and outflow channel length;
2. Tip gap study;
3. Sensitivity of the turbulence model.

A mesh sensitivity study was carried out as well, and we concluded that further refinement of the mesh has no effect on the speed line.

7.1. Sensitivity of the Inflow and Outflow Channel Length

The channel length has a strong influence on both the total pressure ratio and the isentropic efficiency since the losses generated through the wall friction are included in both definitions (see Figure 9). The colored lines represent the CFD calculations with different calculational domains with the corresponding colors in Figure 8a. More than 1% efficiency is lost (from 92% to 91%) due to the long channel.

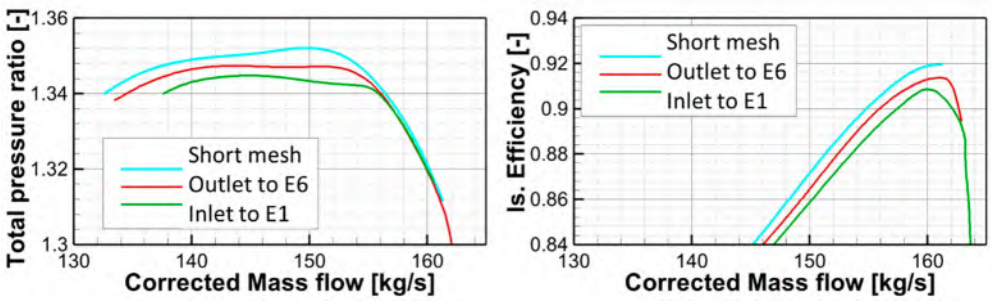

Figure 9. Effect of the considered flow path length on the characteristics (see Figure 8a for colors).

7.2. Tip Gap Study

The study of the tip clearance shows a similar effect (see Figure 10).

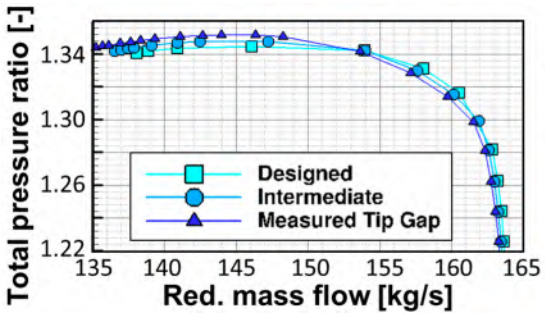

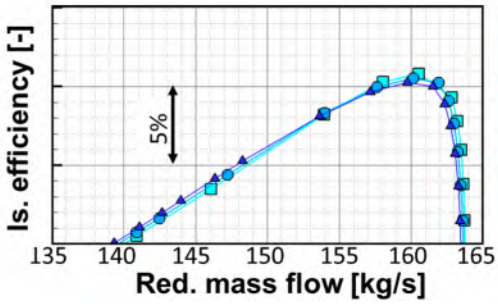

Height (mm)	R1	R2
Designed	0.65	0.5
Intermediate	1.00	1.00
Measured	1.38	1.65

Figure 10. Effect of the tip gap on the performance.

The measured tip clearance for rotor 1 and rotor 2 at 100% speed is about 1.38 mm and 1.65 mm instead of the designed gap of 0.65 mm and 0.5 mm. The reason for this high tip gap is the grinding at the abrasive layer in the rotor case during the commissioning phase. Due to the high tip gap, the efficiency lost a further 0.5%.

7.3. Sensitivity of the Turbulence Model

In the last numerical study, the effect of the selected turbulence model was examined. Significant differences can be observed between the Wilcox k-ω and Menter SST k-ω models [8] (see Figure 11). The achieved Π_{tot} is much lower (1.5%) than with the Wilcox k-ω model. The last calculated point on the speed line is near the maximal Π_{tot} with the SST model, so the speed line is shorter and the agreement with the measured speed line (Experiment) is much better. The flow field of the last calculated point is plotted with the v_{ax} and TKE contours on an x-θ plane at h_{rel} = 0.95. The separation appears on rotor 2, which corresponds with the method to identify the last measured point: the increased vibration on rotor 2 signals the separation. The Wilcox k-ω model appears to be more robust towards separations.

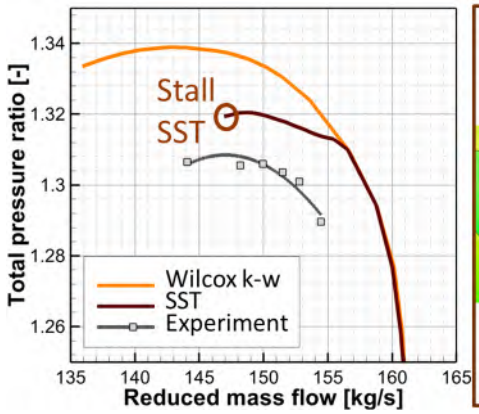

(**a**)

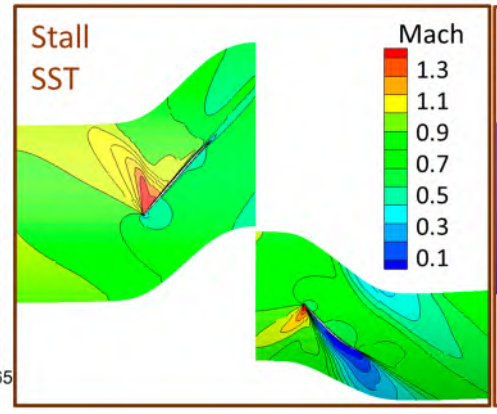

(**b**)

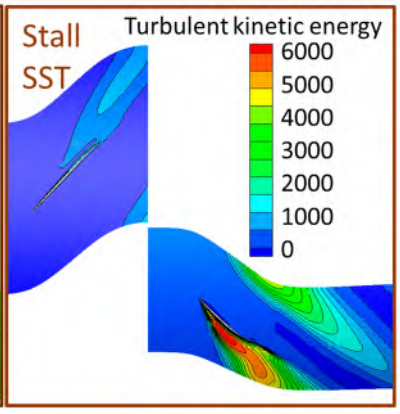

(**c**)

Figure 11. Effect of the turbulence model on the speed line, comparison with the measured 100% speed line (**a**), v_{ax} and TKE contours in the Stall SST point at h_{rel} = 0.95 (**b**,**c**).

As a conclusion of the numerical studies, we can state that the most suitable numerical setup resulted from applying the Menter SST model with the extended calculational domain and tip gap. However, the performance map with all measured speeds was calculated with both turbulence models to see the general effects. In Figure 12, the simulation results are plotted by solid lines for the Menter SST model and by dashed lines for the Wilcox

k-ω model. The measured points are shown only with symbols. The different colors indicate different speeds. It can be stated that the optimized ADP was confirmed by the measurement. The maximal deviation in the mass flow is about 1.2%. The possible reason for this could be the uncertainty of the static pressure measurement if this is not constant in the plane of the BLRs due to the upstream effect of the spinner or other disturbances. The maximal total pressure discrepancies are found at 100% speed. The achieved Π_{tot} is about 0,7% lower as calculated. The explanation for this could be the different geometry or the hub clearance, which will be considered in the detailed evaluation.

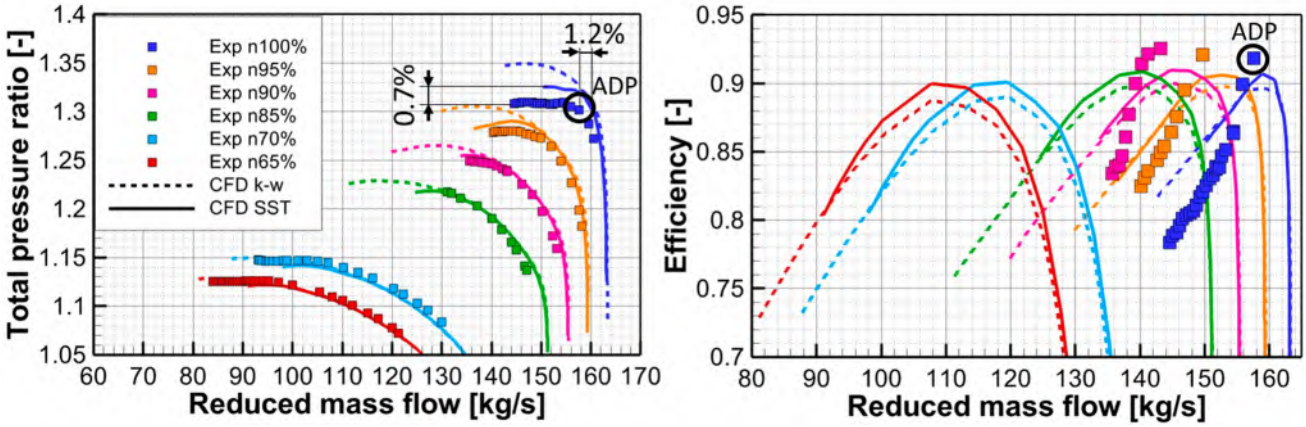

Figure 12. Comparison of the measured and calculated performance maps.

The isentropic efficiency is difficult to determine by temperature measurement for low-pressure-ratio fans due to the uncertainties of the recovery factor, cooling effect, labyrinth seal, etc. Since the exit rakes are installed in the axial direction, the high exit swirl in off-design conditions also has an influence on the quality of the measured temperatures. That is why only the results for the high speeds are shown in the diagram. The most reliable efficiency value is 91.8% at ADP, which is comparable with the calculated 90.7% under test rig conditions.

Finally, the measured and calculated radial pressure and temperature distributions are compared in Figure 13 for the 100% speed and in Figure 14 for the 65% speed. The measured operating points are marked with numbers (1–5) and the simulated points with letters (a to f). A good agreement can be observed between the corresponding points 5-e and 4-d, especially in the gradients of the curves. At the near-stall point "1", the pressure is still increased until 70% blade height but decreased in the tip region. This indicates the beginning of the separation, which can also be seen in the CFD. The error bars are plotted on the radial temperature distribution to show the higher failure at low speed. In Figure 14, the measured operating point "2" is compared with the calculated point "c" in detail. Despite the really good agreement in the pressure and temperature distributions between the points "2" and "c", the efficiency cannot be determined correctly since the small temperature uncertainty of 1 K has also a strong influence on the efficiency at such a low pressure ratio.

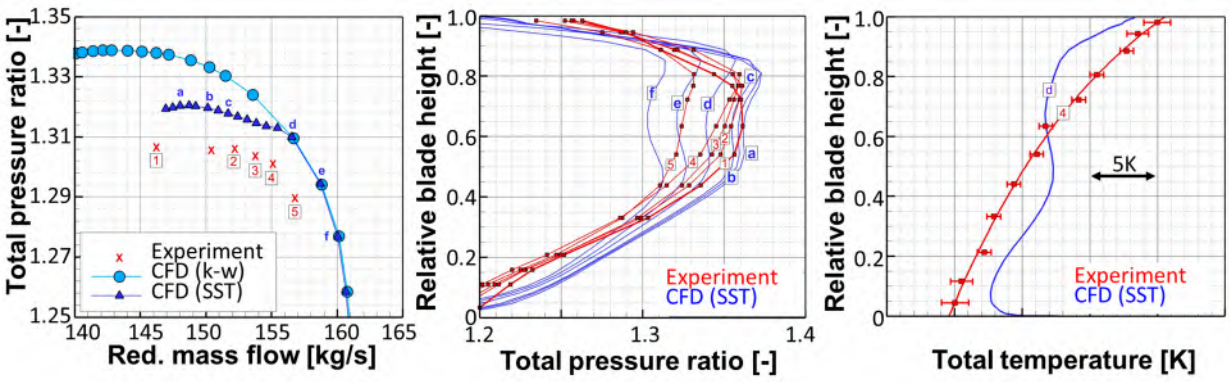

Figure 13. Measured and calculated radial p_t and T_t distributions (100% speed line).

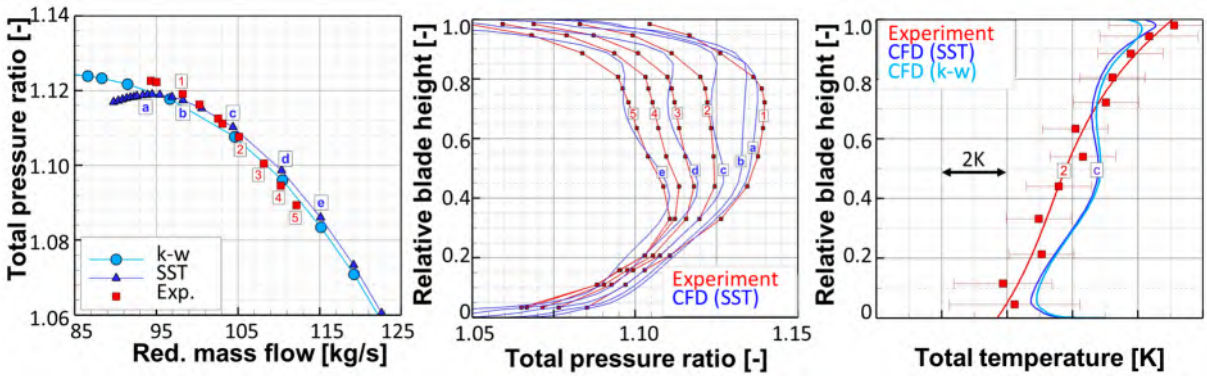

Figure 14. Measured and calculated radial p_t and T_t distributions (65% speed line).

8. Conclusions

Experimental investigations on a counter-rotating fan have been presented here. The aim of this paper was to show the validation results of the performance lines of the fan rig based on the measurement. The numerical studies have shown that the length of the calculational domain, the tip gap height and the selected turbulence model have the most influence on the performance line. Thus, it was confirmed that the objectives of the CRISPmulti project could be achieved. An extensive experimental database was generated for the validation of the numerical methods, which can be evaluated in the future. The effect of the inlet distortion on the fan will be analyzed in detail based on these data in further publications. Not only the aerodynamic properties but also the mechanical and aeroelastic design goals of the blades were confirmed through the experimental investigations of the CRISPmulti test rig.

Author Contributions: Conceptualization, instrumentation and design process, T.L.-K.; validation, G.C.; experimental support, J.K.; structural analysis, P.W.; writing—original draft preparation, T.L.-K. All authors have read and agreed to the published version of the manuscript.

Funding: This research received no external funding.

Institutional Review Board Statement: Not applicable.

Informed Consent Statement: Not applicable.

Data Availability Statement: Blade geometry and measured data are available upon request to the correspondent author.

Acknowledgments: The authors would like to thank the M2VP team for the support in the experimental work.

Conflicts of Interest: The authors declare no conflicts of interest.

Abbreviations

ADP	Aero Design Point
BLR	Boundary layer rake
CRISP	Counter-Rotating Integrated Shrouded Propfan
CFRP	Carbon Fiber-Reinforced Plastic
IPCT	Image Pattern Correlation Technique
M2VP	Multistage Two-Shaft Compressor Test Facility
m	Mass flow
π	Pressure ratio
η_{is}	Isentropic efficiency
R_k	Recovery factor
T	Temperature
p	Pressure

References

1. Sieber, J. *Aerodynamic Design and Experimental Verification of an Advanced Counter-Rotating Fan for UHB Engines*; Third European Propulsion Forum: Paris, France, 1991.
2. Schimming, P. Counter Rotating Fans—An Aircraft Propulsion for the Future? *J. Therm. Sci.* **2003**, *12*, 97–103. [CrossRef]
3. Goerke, D.; Le Denmat, A.-L.; Schmidt, T.; Kocian, F.; Nicke, E. Aerodynamic and Mechanical Optimization of CF/PEEK Blades of a Counter Rotating Fan. In Proceedings of the ASME Turbo Expo 2012: Turbine Technical Conference and Exposition, Copenhagen, Denmark, 11–15 June 2012.
4. Kajasa, B.; Lengyel-Kampmann, T.; Meyer, R. Numerical and Experimental Design of a radial displaceable Inlet Distortion Device. In Proceedings of the ISABE Conference, Ottawa, ON, Canada, 25–30 September 2022.
5. Forsthofer, N.; Reiber, C. Structural Mechanic and Aeroelastic Approach for Design and Simulation of CFRP Fan Blades. In Proceedings of the ASME Turbo Expo, Braunschweig, Germany, 13–15 September 2016.
6. Willert, C.; Klinner, J.; Schroll, M.; Lengyel-Kampmann, T. Measurement of Aerodynamically Induced Blade Distortion on a Shrouded Counter-Rotating Prop-Fan. In Proceedings of the 20st International Symposium on Applications of Laser and Imaging Techniques to Fluid Mechanics, Portugal, Lisbon, 11–14 July 2022. Available online: https://www.lisbonsimposia.org/ (accessed on 12 December 2023).
7. Meyer, R.; Tapken, U.; Klähn, L.; Behn, M.; Rudolphi, A. Experimentelle Untersuchung der Auswirkung von Grenzschichteinsaugung auf die Zuströmturbulenz und die Aeroakustik des gegenläufigen Fan-Modells CRISPMulti. In Proceedings of the Deutsche Luft-und Raumfahrtkongress, Dresden, Germany, 27–29 September 2022.
8. Menter, F.R. Two-equation eddy-viscosity turbulence models for engineering applications. *AIAA J.* **1994**, *32*, 1598–1605. [CrossRef]